





Modern Physics Letters B  
(2023) 2342013 (14 pages)  
© World Scientific Publishing Company  
DOI: 10.1142/S0217984923420137



## Plasmon-associated DNA genotyping based on crystalline assemblies of metallic carbon nanotubes

H. V. Grushevskaya <sup>\*,¶</sup>, V. P. Egorova<sup>†</sup>, N. G. Krylova <sup>‡</sup>, A. S. Babenka <sup>§</sup>  
and G. G. Krylov <sup>\*</sup>

<sup>\*</sup>Physics Department, Belarusian State University,  
4 Nezalezhnosti Ave., 220030 Minsk, Belarus

<sup>†</sup>Belarusian State Pedagogical University,  
Sovetskaya Str. 18, 220030 Minsk, Belarus

<sup>‡</sup>Belarusian State Agrarian Technical University,  
99 Nezalezhnasti Ave., 220012 Minsk, Belarus

<sup>§</sup>Belarusian State Medical University,  
83 Dzerzhinski Ave., 220116 Minsk, Belarus  
<sup>¶</sup>grushevskaja@bsu.by

Received 16 October 2023

Accepted 23 October 2023

Published

Sensitivity and selectivity of modern electrochemical genotyping methods are insufficient to detect a single-oligonucleotide mismatch in low-concentration native DNA samples. Novel methods of tuning, controlling, and monitoring plasmon modes are necessary to achieve attomolar and higher sensitivity for the modern graphene-based transducers of molecular signals. The electrochemical DNA assay is promising one for applications in the molecular diagnostics of tumors with the genome single-nucleotide polymorphism (SNP) for simultaneously discriminating both wild-type and mutant alleles of the gene in very small concentrations. We offer the plasmon-associated DNA-genotyping method based on the screening effects in assemblies of Raman-optically active conjugates comprising DNA and metallic carbon nanotubes. The impedimetric DNA sensors of non-Faradaic type based on the plasmonic screening effect can be more sensitive than the Raman optical transducer based on Raman DNA optical activity resulting in the plasmon resonance due to liability of the Raman transducer parameters to environmental influence.

**Keywords:** DNA-carbon nanotube conjugates; crystalline assemblies of carbon nanotubes; KRAS gene polymorphism; Raman spectroscopy; DNA optical activity; non-Faradaic EIS.

### 1. Introduction

Nowadays, plasmonic and electrochemical DNA assays are promising ones for applications in the molecular diagnostics of tumors with genome single-nucleotide polymorphism (SNP). However, sensitivity and selectivity of modern genotyping electrochemical methods are low to detect allele SNP of cancer genome because of

<sup>¶</sup>Corresponding author.

*H. V. Grushevskaya et al.*

insufficient limit of detection (LOD) for recording point mutations in gene alleles,<sup>1</sup> insufficient LOD when using long DNA probes,<sup>2</sup> and sufficiently high value of guanine and adenine oxidation potentials.<sup>3</sup> Novel methods of tuning, controlling, and monitoring plasmon modes are necessary to achieve attomolar and higher sensitivity for the modern graphene-based transducers of molecular signals. The major difficulties to develop the plasmon-associated graphene-based DNA electrochemical impedance spectroscopy (EIS) for determination of tumor biomarkers are related to confining of the negatively charged target and probe DNA sequences in the near-electrode layer and, vice versa, non-specific nucleotide sequences, including perfect-matched ones chemically bonded with proteins and each others, have to be ejected from the Helmholtz double layer. Development of electrochemical graphene-based transducers based on the plasmon-associated screening effects would allow to enhance the accuracy of modern sequencers about 100 times.<sup>4</sup>

Our goal is to develop a plasmon-associated label-free DNA-genotyping method based on the screening effects in conjugates comprising DNA and crystalline assemblies of few-walled metallic carbon nanotubes.

## 2. Materials and Methods

### 2.1. Target dsDNAs

Native genomic dsDNA was isolated from the formalin-fixed paraffin-embedded samples of colorectal cancer tumor and human placenta. Circulating tumor DNA (ctDNA) was isolated from the blood of patients with colorectal cancer. The placental dsDNA is denoted by dsDNA<sub>pl</sub>. Amplicons of the human KRAS gene has been synthesized by Taq DNA-polymerase. The total volume of the polymerase chain reaction (PCR) mixture was 25  $\mu$ l. The reaction mixture consists of 50 ng of total DNA fraction, 0.5  $\mu$ M of each oligonucleotide, including TaqMan probes for PCR, 0.2 mM of each dNTP, 166 mM (NH<sub>4</sub>)<sub>2</sub>SO<sub>4</sub>, 650 mM Tris-HCl (pH 8.8), 0.2% Tween 20, 2 mM MgCl<sub>2</sub> and 1.25 ME Taq DNA-polymerase. PCR cycling conditions were as follows: 5 min at +95°C, followed by 45 cycles of 10 s at +95°C, 60 s at +60°C. DNA copy (cDNA) from a mRNA template was synthesized by reverse transcription (RT) of the total RNA isolated from the colorectal cancer tumor samples by standard commercial spin-column-based kits. The RT PCR is catalyzed by the reverse transcriptase enzyme.

The following SNP: c.35G>A site, p.G12D, located in the second exon of the human KRAS gene (NCBI/Gene KRAS genomic DNA sequence NC\_000012.12; NCBI/Gene KRAS mRNA var d sequence NM\_001369787.1), is genotyped.

### 2.2. Oligonucleotide probes

The single stranded 19- and 20-base oligonucleotides, KRAS<sub>w</sub> and KRAS<sub>m</sub>, purchased from "Primetech ALC" (Minsk, Belarus) were utilized as primers. The perfectly-matched (KRAS<sub>w</sub>) and single base-mismatched (KRAS<sub>m</sub>) probes are

*Plasmon-associated DNA genotyping based on crystalline assemblies*

complementary to the KRAS-gene wild-type (normal, non-mutant) and mutant-type nucleotide sequences, respectively. KRAS<sub>w</sub> structure (5' → 3') is GTTGGAGCTGGTGGCGTAG, and KRAS<sub>m</sub> structure (5' → 3') is AGTTGGAGCTGATGGCGTAG. The oligonucleotides KRAS<sub>w</sub> and KRAS<sub>m</sub> are distinguished by the nucleotide change in 12th position.

### **2.3. Langmuir–Blodgett sensitive films**

A sensitive layer of the electrochemical-transducer is constructed with few-walled carbon nanotubes (FWCNTs). The original FWCNTs with diameters ranging from 1.0 and less to 5 nm and length of  $\sim 2.5 \mu\text{m}$  have been synthesized using a method of chemical vapor deposition (CVD-method).<sup>5</sup> Then, FWCNTs were covalently modified by carboxyl groups and mixed with a DNA probe and stearic acid in hexane. Inverse stearic-acid micelles of the conjugates DNA probe–CNT were fabricated by ultrasonic irradiation of the mixture. Monomolecular crystalline layers of the non-covalently stearic-acid-functionalized micellar conjugates (DNA–CNT-conjugate crystalline monolayers) were fabricated by employing the Langmuir–Blodgett (LB) technique. The monolayers were formed by compressing a two-dimensional gas of the inverse stearic-acid micelles with the carboxylated FWCNTs and DNA probe molecules inside. Then, the two LB monolayers were deposited onto surface of interdigital electrode structures which were isolated by nanoporous anodic aluminum oxide (AAO) with pores of 10 nm in diameter. Preliminary, Ce- and/or iron-containing 5-monolayer LB films of an amphiphilic oligomer of thiophene derivatives with chemically bounded hydrophobic 16-link hydrocarbon chain denoted as H-DTP were fabricated and deposited on AAO. A chemical structure of H-DTP is 3-hexadecyl-2,5-di(thiophen-2-yl)-1H-pyrrole. (see Ref. 6 and references therein). The working solution of H-DTP, 1.0 mM, was prepared by dissolving precisely weighted substances in hexane. As a result, the DNA probe–CNTs were decorated by the nanocyclic organometallic LB-complexes of octahedral high spin Fe(II).<sup>7–9</sup> Salts Fe(NO<sub>3</sub>)<sub>3</sub> · 9H<sub>2</sub>O, Ce<sub>2</sub>(SO<sub>4</sub>)<sub>3</sub> (Sigma, USA), hydrochloric acid, deionized water with resistivity of 18.2 MΩ·cm were used to prepare subphases. All chemical reagents of analytical grade were used without further purification.

### **2.4. Electrochemical impedance spectroscopy**

Electrophysical studies have been performed using planar interdigital electrode structures on a pyroceramics support.  $N$  pairs,  $N = 20$  of aluminum electrodes are arranged in an Archimedes-type spiral configuration. Every such a pair is an “open-mode type” capacitor. To excite harmonic auto-oscillations of electric current (charging–discharging processes in the capacitors), the sensor was connected as the capacitance  $C$  into the relaxation resistance ( $R$ ) – capacitor ( $C$ ) oscillator (self-excited  $RC$ -oscillator).<sup>10</sup> Operating of such  $RC$ -generator is based on the principle of self-excitation of an amplifier with a positive feedback on a quasi-resonance frequency. The capacitance  $C$  of the sensor entered in measuring  $RC$ -oscillating circuit

*H. V. Grushevskaya et al.*

has been calculated by the formula  $C = 1/(2\pi Rf)$ , where  $R$  is the measuring resistance,  $f$  is the frequency of the quasi-resonance.

EIS measurements have been made with a BORDO-322 digital oscilloscope (UniTechProm, Minsk, Belarus) which provides automatic measurements and mathematical signal processing (fast Fourier transforms) of the harmonic electrical signals.

All electrochemical measurements are performed in deionized water.

### 2.5. Raman spectroscopy

Spectral studies in visible range were carried out using a confocal micro-Raman spectrometer Nanofinder HE (“LOTIS-TII”, Japan–Belarus) on diode-pumped solid-state (DPSS) lasers operating at wavelengths of 473 nm and 532 nm with the power in the range from 0.0001 mW to 20 mW. The spectra were recorded in the back-scattering geometry under a  $\times 50$  objective at room temperature (RT). The size for the optical image is of  $7 \times 7 \mu\text{m}$ , vertical spatial resolution 150 nm, spectral resolution is of up to 0.01 nm.

### 2.6. Statistics

Each individual signal of the genosensor is registered not less than 60 times as a response of the sensor has been detected more than 30 times at different frequencies  $f$  and not less than twice for each value of measuring resistance  $R_{ns}$ . An effective standard deviation,  $\sigma_\Sigma$ , for an integral value,  $C_\Sigma$ , of the capacitance is determined as follows. First, a moving average filter,  $\mu(f)$ , has been constructed for a linear interpolation of the experimental Bode plot consisting of all  $N_B$  experimental points. Each point of the filter has been found by averaging over five linear-interpolation points, being distant from each other by 35 kHz. The points in the filter are spaced by 1 kHz. Second,  $N_B$  moving average filters,  $\mu_{P,i}(f)$ ,  $i = 1, \dots, N_B$ , have been constructed for linear interpolations of  $(N_B - 1)$  experimental points with the following construction of a linear interpolation  $\mu_i(f)$  over  $\mu_{P,i}(f)$  and the  $i$ th non-average experimental point. Then, the effective standard deviation has been calculated by the following formula:

$$\sigma_\Sigma = \left[ \frac{1}{N_B - 1} \sum_{i=1}^{N_B} (\mu_{\Sigma,i} - \mu_\Sigma)^2 \right]^{1/2} \quad (1)$$

where  $\mu_{\Sigma,i}$  and  $\mu_\Sigma$  are integral values of  $\mu_i(f)$  and  $\mu(f)$ . An effective relative standard deviation (RSD) for the Bode plot  $C(f)$  has been calculated as a ratio of the effective standard deviation to the mean integral value,  $\mu_\Sigma$ , of capacitance. RSD for all experiments was from 0.003% to 0.02%.

The hybridization signal  $\Delta C_\Sigma$  is determined as the following difference:  $\Delta C_\Sigma = C_{\Sigma,ah} - C_{\Sigma,bh}$  between integral values,  $C_{\Sigma,ah}$  and  $C_{\Sigma,bh}$ , of the capacitances,  $C_{ah}(f)$  and  $C_{bh}(f)$ , after and before hybridization, respectively.

The dsDNA<sub>pl</sub> was used as a non-template negative control. Sensitivity of the electrochemical genotyping was assessed by comparing the integral values of electrochemical signal outputs from the target-dsDNA samples and the dsDNA<sub>pl</sub>-KRAS<sub>w</sub> against the dsDNA<sub>pl</sub>-KRAS<sub>m</sub> assays. The sensitivity was evaluated by the Student's *t*-test that determines statistical significance or difference (*P*-value).

### 3. Results

#### 3.1. Theory of dielectric losses in capacitive DNA-hybridization transducer

Operating principles of the non-Faradaic impedimetric DNA-hybridization sensors are based on changes in the complex dielectric permittivity,  $\epsilon = \epsilon' + i\epsilon''$ , of the near-electrode Helmholtz layer.

When inducing the charge density,  $\delta n$ , an applied electric field,  $\mathbf{E}$ ,  $\mathbf{E} = -\text{grad } U$ , (bias,  $U$ ) is screened by the conducting LB-film that, accordingly Maxwell equations<sup>11</sup> the electric displacement vector,  $\mathbf{D} = \{D_i\}_{i=1}^3$ , arises as

$$\begin{aligned} \text{div } \mathbf{D} &= \epsilon_0 \text{div } \mathbf{E} - e\delta n = en^{\text{ext}} = \epsilon_0 \\ &\times \text{div} \left( \mathbf{E}(\mathbf{r}, t) + \sum_j \int dt' d\mathbf{r}' \mathbf{K}_j(\mathbf{r} - \mathbf{r}', t - t') E_j(\mathbf{r}', t') \right), \end{aligned} \quad (2)$$

where  $en^{\text{ext}}$  is an external charge density  $e$  is the electron charge. The Maxwell equation (2) describes the response which is determined by the  $j$ th vector  $\mathbf{K}_j$ ,  $j = 1, 2, 3$  of response functions as  $\mathbf{K}_j = \{K_{ij}\}_{i=1}^3 = \{K(\mathbf{r}, t)\delta_{ij}\}_{i=1}^3$ , this response is one to Coulomb interaction after Fourier and Laplace transformations, the response to a harmonic signal  $\mathbf{E}(\omega, q)$  with a frequency  $\omega$  and wave number  $q$  can be represented through the complex dielectric permittivity,  $\epsilon(\omega, q)$ , as

$$\begin{aligned} \mathbf{D}(\omega, q) &= \epsilon_0 \epsilon(\omega, q) \mathbf{E}(\omega, q) = \epsilon_0 \\ &\times \left( 1 + \int_0^\infty d\tau \int d\mathbf{p} e^{-i(\mathbf{q}\mathbf{p} - \omega\tau)} K(\mathbf{p}, \tau) \right) \mathbf{E}(\omega, q) \end{aligned} \quad (3)$$

and is described by the following Fourier–Laplace image of the Maxwell equation as

$$\begin{aligned} \mathbf{q} \cdot \mathbf{D}(\omega, q) &= \epsilon_0 \epsilon(\omega, q) \mathbf{q} \cdot \mathbf{E}(\omega, q) = en^{\text{ext}}(\omega, q) \\ &= \epsilon_0 \mathbf{q} \cdot \mathbf{E}(\omega, q) - e\delta n(\omega, q). \end{aligned} \quad (4)$$

The last gives the induced charge density

$$-\delta n(\omega, q) = \frac{\epsilon(\omega, q) - 1}{\epsilon(\omega, q)} n^{\text{ext}}. \quad (5)$$

Then, for the harmonic signal depending on the frequency  $\omega$  and wave number  $q$ , the Fourier–Laplace image of this response consists in appearance of a Coulomb

*H. V. Grushevskaya et al.*

field of induced charge  $V$ , as

$$\frac{V(q, \omega)}{1 - \epsilon(\omega, q)} = \frac{U^{\text{ext}}(q, \omega)}{\epsilon(\omega, q)}. \quad (6)$$

Here,  $U^{\text{ext}}$  and  $V$  being equal to  $\frac{\epsilon n^{\text{ext}}(q, \omega)}{q^2}$  and  $\frac{\epsilon \delta n(q, \omega)}{q^2}$ , respectively, are Fourier images of solutions of corresponding Poisson equations. A screened Coulomb potential,  $U^{\text{screen}} = U^{\text{ext}}/\epsilon(\omega, q)$ ,<sup>12</sup> charges the capacitor due to the polarization  $\mathbf{P}$ ,  $\mathbf{P} = \Pi(\mathbf{E} + \mathbf{P})$ .<sup>13</sup> Here  $\Pi$ ,  $\Pi = N\alpha$  being the polarizability per unit volume satisfies the Clausius–Mossotti equation  $\Pi = 3\frac{\epsilon_c - 1}{\epsilon_c + 2}$ ;  $\epsilon_c$  is the dielectric constant,  $N$  is a number of molecules per unit volume,  $\alpha$  is the polarizability per molecule. Accordingly to the formula (6), since  $\mathbf{P} = -\Pi \text{grad } U^{\text{screen}}$ , the bias  $V$  is equal to

$$\text{grad } V = \frac{\epsilon - 1}{\Pi} \mathbf{P} \equiv \frac{(\epsilon - 1)(1 - \Pi)}{\Pi^2} \text{grad } U. \quad (7)$$

The bias  $U$  gives rise to  $I_{ch}$  and  $\Pi \approx 3$  because the dielectric constant for water is large and, correspondingly,  $\epsilon_c \sim 81$ . Then, the discharging (charging) current is proportional to the following expression:

$$I_{ch} \sim \frac{9}{2} \frac{V}{1 - \epsilon}. \quad (8)$$

The imaginary part,  $\epsilon''$ , of the complex dielectric permittivity presents a resistivity because<sup>14</sup>

$$\epsilon = 1 + i \frac{\sigma}{\epsilon_0 \omega}. \quad (9)$$

Here,  $\sigma$  is the complex conductivity,  $\omega$  is the cyclic frequency. It follows from the last equation and Eq. (8) that

$$I_{ch} \sim \Im m \frac{V}{1 - \epsilon} \sim \Re e \frac{\epsilon_0 \omega V}{\sigma} \sim \frac{V}{\epsilon''}. \quad (10)$$

But, the energy  $CV^2/2$  stored at (released from) the capacitance  $C$  is determined by the following expression:  $CV^2/2 \sim I_{ch}V$ . Substituting the expression (10) for the  $I_{ch}$  into the expression for the energy one gains that  $\epsilon'' \sim 1/C$ . The last signifies that the dielectric losses  $\epsilon''$  due to the dielectric-polarization relaxation process occur in a frequency range where the sensor capacitance  $C$  falls down.

### 3.2. Raman spectral studies of micellar dsDNA

A sensitive layer of the hybridization transducer comprises micellar DNA primary entering micellar DNA–CNT conjugates from inverse micelles of stearic acid. Let us make comparison between Raman spectra of dried dsDNA and the dsDNA inside of stearic-acid micelles. Results of the Raman spectral analysis is in Table 1. The Raman bands for the native dried and micellar dsDNAs mainly are related to Raman spectra for dsDNA in A form, that forms a tighter helix than dsDNA in B form. However, Raman peaks attributed to disordered regions of the bulk dsDNA are

*Plasmon-associated DNA genotyping based on crystalline assemblies*

Table 1. Characteristic molecular vibrations, observed in the Raman spectra of native dsDNA in different forms.

Raman bands, $\text{cm}^{-1}$			
Dried placental DNA	Micellar placental DNA	Dried calf DNA <sup>15,16</sup>	Assignment
663.6	—	663	665 $\text{cm}^{-1}$ for C-3'-endo-anti ring pucker for Gu entering Gu-Cy dsDNA in A form <sup>17</sup> ; 666 $\text{cm}^{-1}$ T in A-form A-T DNA <sup>17</sup> ; 680–656 $\text{cm}^{-1}$ for in-phase ring stretching vibration of Gu. <sup>18</sup>
728.2 (disordered)	—	727 (disordered)	728 $\text{cm}^{-1}$ for A of A-T disordered dsDNA <sup>17</sup> ; 724–732 $\text{cm}^{-1}$ for in-phase ring stretching vibration of A. <sup>18</sup>
—	—	742	T, d <sup>15,16</sup>
783	—	783	783 $\text{cm}^{-1}$ for vibrations of deoxyribose phosphate backbone (bc) and Cy in Gu-Cy A-form dsDNA <sup>17</sup> ; 790–796 $\text{cm}^{-1}$ for in-phase ring stretching vibration of Cy. <sup>18</sup>
802 (A-form)	835 (B form)	—	807 $\text{cm}^{-1}$ and 808 $\text{cm}^{-1}$ is values of frequencies of C-3'-endo-furanose-ring pucker for bc of A-T and Gu-Cy A-form DNAs, respectively <sup>17</sup> ; 841 $\text{cm}^{-1}$ is a very weak band from C-2'-endo-furanose-ring pucker for A-T dsDNA in B form. <sup>17,19</sup>
881.6	880	—	852 $\text{cm}^{-1}$ is a frequency of bc vibration for Gu-Cy dsDNA in A form. <sup>17</sup>
963.6	920	—	960 $\text{cm}^{-1}$ for rocking $\text{NH}_2$ and stretching $\text{N}=\text{C}$ of A <sup>18</sup> ; 920 $\text{cm}^{-1}$ for A in A-form dsDNA.
1014	1020	1012	1020 for rocking $\text{NH}_2$ and stretching CH in Cy. <sup>18</sup>
1060.64	1050	1060	d(CO). <sup>15,16</sup>
1100	1100	1100	phosphodiester bond DP( $\text{PO}_2^-$ ) of dsDNA in A form. <sup>15,17</sup>
1141.25	1140	—	1140 $\text{cm}^{-1}$ for stretching ( $-\text{NH}$ ) and bending CH in Cy. <sup>18</sup>
1181.3	—	1181	1180 $\text{cm}^{-1}$ for Gu, Cy in A- and B-form Gu-Cy dsDNA. <sup>17</sup>
—	1185 (B form)	—	1186 $\text{cm}^{-1}$ for T in disordered and B-form A-T dsDNA <sup>17</sup> ; 1184–1169 $\text{cm}^{-1}$ for bending ( $-\text{CH}$ ) and stretching CN in T. <sup>18</sup>
1208.9 (disordered)	—	—	1208 $\text{cm}^{-1}$ , 1209 $\text{cm}^{-1}$ for T, A in disordered and B-form A-T dsDNA, respectively; not resolvable for A-form dsDNA. <sup>17</sup>
1245.67	1245	1243	1242 $\text{cm}^{-1}$ for Cy of Gu-Cy dsDNA in A-form. <sup>17</sup>
—	1270	—	1295 $\text{cm}^{-1}$ for Cy in A-form Gu-Cy dsDNA <sup>17</sup> ; 1294–1306 $\text{cm}^{-1}$ for a N-C stretch coupled to C=C stretching in Cy. <sup>18</sup>
1303.53	1300	1308	1301 $\text{cm}^{-1}$ A in A-form A-T dsDNA. <sup>17</sup>
1344 (B form)	1340 (A-form)	1335	1334 $\text{cm}^{-1}$ for A in disordered and A-form A-T dsDNAs <sup>17</sup> ; 1341 $\text{cm}^{-1}$ for A entering B-form A-T dsDNAs. <sup>17</sup>

H. V. Grushevskaya et al.

Table 1. (Continued)

Raman bands, $\text{cm}^{-1}$			
Dried placental DNA	Micellar placental DNA	Dried calf DNA <sup>15,16</sup>	Assignment
1373.1	1370	1372	1374 $\text{cm}^{-1}$ for T, A in A-form A-T dsDNA <sup>17</sup> ; 1362–1370 for stretching (C=N) and (N-C) groups in A <sup>18</sup> ; 1372–1388 $\text{cm}^{-1}$ for bending (C-Me) of T. <sup>18</sup>
1418.2	1418	1418	1418 $\text{cm}^{-1}$ for a C=N stretch coupled to NH <sub>2</sub> stretching in Gu <sup>18</sup> ; 1417 $\text{cm}^{-1}$ for A, Gu, bc entering A-form A-T and Gu-Cy DNAs. <sup>17</sup>
1484 (disordered)	shoulder 1480 (A-form)	1484 (disordered)	1482 $\text{cm}^{-1}$ and 1486 $\text{cm}^{-1}$ for Gu in A-form and disordered Gu-Cy dsDNA, respectively <sup>17</sup> ; 1478 $\text{cm}^{-1}$ for A in A-form DNA <sup>17</sup> ; 1483 $\text{cm}^{-1}$ for A in disordered and B-form DNAs <sup>17</sup> ; 1488 $\text{cm}^{-1}$ for stretching group C-N-C in Gu. <sup>18</sup>
1504.8	1500	1508	1503–1504 $\text{cm}^{-1}$ for bending NH group of T. <sup>18</sup>
1528.6 (disordered)	1520 (A-form)	1528 (disordered)	1528 $\text{cm}^{-1}$ for Gu in disordered Gu-Cy dsDNA <sup>17</sup> ; 1538 $\text{cm}^{-1}$ for a (C=C) stretch coupled to C-N stretching in Gu <sup>18</sup> ; 1520 $\text{cm}^{-1}$ for Gu in A-form dsDNA.
1573	1570	1574	1574 $\text{cm}^{-1}$ for Gu in A-form Gu-Cy dsDNA <sup>17</sup> ; 1576–1582 $\text{cm}^{-1}$ for C-N stretch coupled to (C=C) stretching in Gu. <sup>18</sup>
shoulder 1600	1607	—	1605 $\text{cm}^{-1}$ for C=N stretch in A <sup>20</sup> ; 1609 $\text{cm}^{-1}$ for NH <sub>2</sub> in dsDNA <sup>20</sup> ; 1655 $\text{cm}^{-1}$ for (C=O) NH in Cy. <sup>18</sup>
1661	1641	1664	Vibration of the group (C=O) NH (called “Amide I”) is a amide C=O stretch coupled to N-H wagging that is of 1632–1670 $\pm$ 2–5 $\text{cm}^{-1}$ <sup>17</sup> for Gu; 1641 $\text{cm}^{-1}$ for Gu entering A-form dsDNA.
2747	2721	—	d(CH).
2894	2845.6, 2880.7	2894	d(CH). <sup>15,16</sup>
2955.36	2921	2950, 2957	d(CH). <sup>15,16</sup>

Notes: Abbreviations used: adenine, guanine, thymine and cytosine are designated by A, Gu, T, and Cy, respectively; d, deoxyribose.

present in the Raman spectra also (see Table 1). It signifies that some sites of the bulk dsDNA are disordered. Contrary to the bulk dsDNAs, both strands of the micellar DNA<sub>pl</sub> are spiral chains. When being stretched, the micellar A helix of some A-T-rich regions transits into the B form. It testifies the appearance the band from C-2'-endo-furanose-ring pucker being feature for A-T dsDNA in B form and the Raman band of 1185  $\text{cm}^{-1}$  being feature for thymine entering B form (see Table 1).

The positions of characteristic bands of the micellar DNA<sub>pl</sub> are shifted to the lower frequency range on respect to that of the dried-DNA<sub>pl</sub>. It signifies that the micellar DNA are more deprotonated than the dried DNA and, correspondingly, an



*Plasmon-associated DNA genotyping based on crystalline assemblies*

extent of conjugation increases in the micellar DNA.<sup>7,8,20,22</sup> Some adenine-rich A-helix regions of the bulk dsDNA can transit into B form. The comparison between the Raman spectra for the bulk human placental and calf-thymus dsDNAs gives that the frequency of  $1208\text{ cm}^{-1}$  is recorded for the bulk DNA<sub>pl</sub>. It indicates that the presence of the bulk B-form DNA<sub>pl</sub> sites is a result of protonation happening in the less dehydrated dsDNA<sub>pl</sub> (see Table 1).

The largest shifts were recorded for the following dried-DNA adenine and guanine peaks:  $963\text{ cm}^{-1}$  and  $1661\text{ cm}^{-1}$ , respectively, for which red wavelength shifts are equal to  $43\text{ cm}^{-1}$  and  $20\text{ cm}^{-1}$ , respectively. Thus, adenine and guanine bases most subject to protonation with subsequent oxidation due to their oxidation potential value being the lowest among the nucleotide oxidation potentials. Impact of deprotonization is that the DNA helical structure and, correspondingly, the conjugation chain is restored. It means that hole conduction appears for the DNA double helix after the reduction of adenine and guanine bases. The least shifts are recorded for the dried-DNA cytosine and thymine peaks. For example, the cytosine and thymine peaks of  $1141.25\text{ cm}^{-1}$  and  $1442\text{ cm}^{-1}$ , respectively, shift to lower frequencies by  $1.25\text{ cm}^{-1}$  and  $4\text{ cm}^{-1}$ , respectively. Thus, cytosine and thymine bases are weakly subject to protonation with subsequent oxidation due to the large values of their oxidation potential.

dsDNA being deposited on CNT surface remains its helical structure. The DNA double helix is optical active.<sup>23-25</sup> It means that the helical DNA on CNT surface circularly polarizes laser radiation. Raman scattering of the circularly polarized electromagnetic quanta in the graphene sheet gives rise to whirling graphene electron density around the zero-energy Majorana mode (vortex core) residing in the Dirac point  $K(K')$ . It brings about the deconfinement of the vortical pseudo Majorana quasi-particles, whose disintegration (the loss of correlation between individual branches of vortex) originates electron-hole pairs of the Dirac fluid. High-intensity collective (plasmonic) oscillations of the graphene charge carriers arise under an action of electrical fields of vibrational DNA molecular groups, and then an elastic scattering of the laser beam on the graphene plasmons occurs resonantly. The intensity of the peaks in the Raman spectrum of dsDNA<sub>pl</sub>-individual-CNT conjugates increase more than twice compared to the intensities of the Raman peaks of the micellar dsDNA in a result of the plasmon resonance.

### ***3.3. Plasmon-associated screening effects in conjugates between metallic carbon nanotubes and DNA***

Graphene hosts zero-energy pseudo Majorana modes in the Dirac points. Plasmon modes in graphene may be originated from the swirling of the graphene electron density as the low- and high-frequency dielectric function (imaginary part of conductivity) is featured by zeros (see Fig. 1(a)).<sup>26</sup> In experiments, the graphene plasmons are excited by circularly polarized quanta of electromagnetic field,<sup>25,27</sup> including that in terahertz range (see Ref. 28 and references therein).

H. V. Grushevskaya et al.

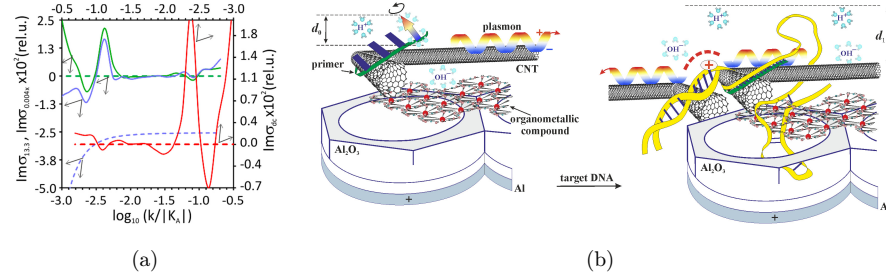


Fig. 1. (Color online) (a) Imaginary part of longitudinal Ohmic conductivity,  $\sigma(\omega, k)$ , of the pseudo Majorana fermions (solid curves) and of Dirac fermions in graphene<sup>32</sup> (dashed curves), versus wave number  $k$ ,  $\mathbf{k} = \mathbf{p} - \mathbf{K}_{A(B)}$  at the temperature 100 K and the frequencies  $\omega$ : 13.3 K (0.27 THz), 0.004 K (83 MHz),  $10^{-10}$  K (2.08 Hz); the chemical potential equals to 1 K.  $\Im m \sigma(\omega, k)$  is measured in the relative unit  $e^2/h$  and labeled as  $\Im m \sigma_{13.3}$  (blue color),  $\Im m \sigma_{0.004}$  (green color), and  $\Im m \sigma_{dc}$  (red color) for the frequencies 13.3, 0.004, and  $10^{-10}$  K, respectively;  $h$  is the Plank constant. (b) A cartoon of operating principle of the electrochemical genotyping.

Dipoles comprising hydrated ions ( $\text{OH}^-$ ) and counterions ( $\text{H}^+$ ), and hydrated dipoles, for example, of nucleotide bases form a Helmholtz double layer. Resonances of water in hydrate-like cages, which is formed by molecules of hydrate water around the dipole, are in the terahertz range and are emitted after the decay of the hydrate complex into the cage and dipole as a result of vibrations (rotation) of the dipoles in an alternating electric field.<sup>29–31</sup> Reorientation of the dipoles of the Helmholtz double layer in the alternating electric field of the electrode is accompanied by the emission of an electromagnetic field in the terahertz range.

Unlike the DNA dipoles, dipoles consisting of hydrated  $\text{OH}^-$  and  $\text{H}^+$  and rotating in an alternating electric field disappear at low electric field strengths due to the association of ions into neutral molecules with the disappearance of the water cages. In the absence of radiation from the cage resonances, electrons and holes in graphene annihilate very quickly so that the only core of the vortex remains (zero-energy pseudo Majorana mode). These processes of confinement and deconfinement of the pseudo Majorana quasi-particles give rise to the CNT electroactivity that is resolved by the Warburg impedance in the CNT dielectric spectrum. Negatively charged regions of the plasmon wave effectively reduce the electrical charge on the electrode as Fig. 1(b), left shows. Correspondingly, by reducing the intensity of the process of water-molecules ionization, this plasmon-associated screening of the electrodes electric field decreases the electrical capacitance of the Helmholtz double layer. The higher the intensity of the plasmonic modes, the better the screening efficiency.

Figure 1(b) depicts the near-electrode Helmholtz layer comprising the conjugates “ssDNA–CNT” and “dsDNA–CNT” before and after hybridization with a perfectly matched chain of target, respectively. The plasmon wave is attenuated when scattered at the CNT ends. Since guanine is reduced during the double helix formation, hole conductivity appears in DNA. Conductive double-stranded DNA regions, linking the CNT ends, create a network of ways along which the graphene plasmons

*Plasmon-associated DNA genotyping based on crystalline assemblies*

can jump from one CNT to another one and, correspondingly, move indefinitely throughout the CNT assembly (make comparison between Fig. 1(b), left and right). Since the area of plasma-wave propagation effectively expands, the intensity of plasmon waves increases. As a result, since the number of oxidized guanines decreases and the number of hydrate complexes is proportional to the electrical charge of the double layer, the capacitance of the latter decreases. But, as one can see, the thickness of the double layer may also decrease after complementary binding if the oxidized guanines of the untwisted regions of the target DNA make a large contribution to the polarization.

Thus, when binding the electroactive conductive substrates the target analyte which is residing in the Helmholtz layer dramatically changes the EIS-impedance.<sup>33–36</sup> The change of capacitance of the electrode–electrolyte interface can be considered as the main indicator of the hybridization interaction. It means that, unlike the Helmholtz layer formed by the dipole-polarized ssDNA, an additional Maxwell–Wagner polarization of the Helmholtz layer with the dsDNA inclusions occurs due to hole conduction of the helicoidal dsDNA.<sup>7</sup> When strongly screening the applied electrical field of the frequency  $\omega$ , the Maxwell–Wagner polarization affects the ion hydrate complexes formation that the capacitance of the double layer decreases.<sup>37</sup>

### ***3.4. Electrochemical KRAS-gene sequencing based on plasmonic conjugates DNA–CNT-assembly***

We present a genotyping electrochemical technology to discriminate a single-nucleotide mutation in the KRAS gene (2 exon, 12 codon, G/A). To recognize the mutant and wild alleles, it was necessary to use two sensors. The wild-type allele detection probe was placed on the surface of the first sensor. The probe for detecting the mutant-type allele was located on the surface of the second sensor. This technology is based on the screening effect leading to that the capacitance values for a wide frequency range decrease as a result of the complementary hybridization between target and probe DNA sequences.

We have sequenced real-time-PCR amplicons and RT-PCR cDNA for the DNA colorectal cancer tumor and the ctDNA from blood of patients with colorectal cancer. The results of their sequencing are shown in Fig. 2. The integral capacitance of all samples decreased, with the exception of the cDNA sample in the concentration of 6.25 ng/ml and for the sensitive layer being decorated by Fe only. The signal output from the cDNA sample in the concentration of 6.25 ng/ml indicates an increase in the electrical capacitance of the sensor due to the predominance of the proportion of the dsDNA in the coiled state over the double-stranded one and, correspondingly, due to a large guanine-dipole contribution. All these samples showed statistical significance for a significance level of 0.02–0.05. All the samples are contaminated however, the molecules being non-specific bonded with DNA probes are easily washed and do not contribute in the transducer response. The Fe–Ce containing sensor covering is preferred as the sensitive transducer layer because the

H. V. Grushevskaya et al.

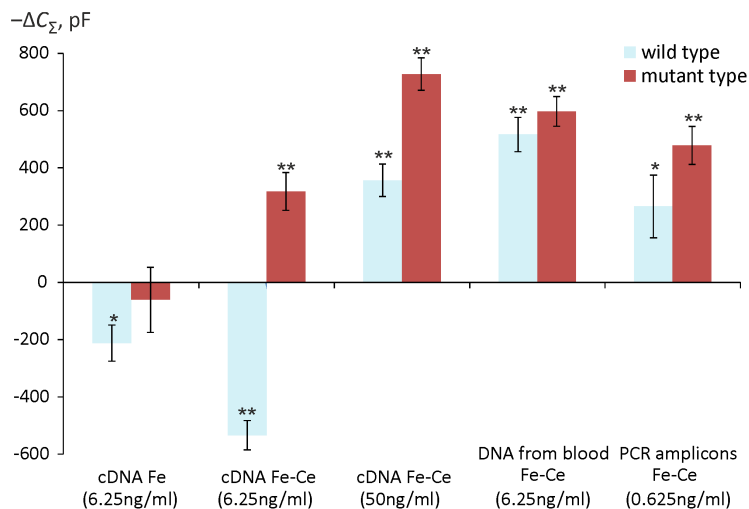


Fig. 2. (Color online) EIS genotypings. Integral values,  $-\Delta C_{\Sigma}$ , of capacitance difference for samples obtained by the method of RT from RNA, isolated from cancer tissue samples of patients (cDNA); for the DNA samples isolated from blood of patients with colorectal cancer (ctDNA); for PCR products (PCR amplicons). The DNA concentration in the measuring cell is indicated in parentheses. Error bars represent threefold standard deviation ( $3\sigma$ ). The statistical significance is as follows:  $**P \leq 0.02$ ;  $*P \leq 0.05$ . “Fe” and “Fe-Ce” designate the type of sensor coating, comprising organometallic iron or iron-cerium complexes, respectively.

helix-coil transition occurs faster in the presence of Ce. Thus, it was found that the genosensor preserves its ability to discriminate allele SNP even in the presence of high concentration of interferences.

#### 4. Discussion and Conclusion

So, the experimental studies performed have revealed that the stacking interactions between  $\pi(p_z)$  electrons of carbon nanotubes and DNA molecules hamper non-complementary hybrid formation. The observed screening effects of DNA hybridization are explained by the topologically nontrivial Majorana origin of the graphene charge carriers. The plasmonic high-ordered DNA-CNT hybrids effectively screen near-electrode double charged layers. Single strands of complementary target DNA penetrate through nanocavities of nanocyclic complexes into the pores of anodic aluminum oxide. Some sites of this penetrated DNA are structured into double-stranded DNA and are confined in the AAO nanopores, since due to the large diameter of the double helix they cannot pass into the volume. Due to the locking of such sites of the target DNA in the AAO pores, the DNA poly-ion does not leave the conjugates between the homoduplexes and CNT when the sign of the electrode electric potential changes to the opposite one. Dielectric and Raman spectral studies of DNA hybridization on surface of crystalline metallic CNT assemblies which are suspended on nanopores have been performed. It has been shown that the


*Plasmon-associated DNA genotyping based on crystalline assemblies*

carboxylated CNTs decorated by the nanocyclic organometallic complexes can be used to discriminate SNP of colorectal tumor genome. We have offered impedimetric DNA sensors of non-Faradaic type based on the plasmonic screening effect.


To summarize our findings. The new high-performance DNA nanosensor has been developed to genotype DNA sequences from colorectal-cancer tumor samples and blood of patients with colorectal cancer. The sensor operation is based on different electrochemical capabilities of the assemblies ssDNA–CNT and the network formed by homoduplexes linking the nanotubes to each other.

## ORCID

H. V. Grushevskaya  <https://orcid.org/0000-0002-9527-9328>

N. G. Krylova  <https://orcid.org/0000-0002-9819-0556>

A. S. Babenka  <https://orcid.org/0000-0002-5513-970X>

G. G. Krylov  <https://orcid.org/0000-0002-5299-9157>

## References

1. L. Li, Sh. Wang, T. Yang, Sh. Huang and J. Wang, *Biosens. Bioelectron.* **33** (2012) 279.
2. M. T. Hwang, P. B. Landon, J. Lee, D. Choi, A. H. Mo, G. Glinsky and R. Lal, *Proc. Natl. Acad. Sci.* **113** (2016) 7088.
3. M. Silvestrini, L. Fruk, L. M. Moretto and P. Ugo, *J. Nanosci. Nanotechnol.* **15**(5) (2015) 3437.
4. D. Rodrigo O. Limaj, D. Janner, D. Etezadi, F. J. G. de Abajo, V. Pruneri and H. Altug, *Science* **349** (2015) 165.
5. V. Labunov, B. Shulitski, A. Prudnikava, Y. P. Shaman and A. S. Basaev, *Semicond. Phys. Quantum Electron. Optoelectron.* **13** (2010) 137.
6. H. V. Grushevskaya, I. V. Lipnevich and T. I. Orekhovskaya, *J. Mod. Phys.* **4** (2013) 7.
7. H. V. Grushevskaya, N. G. Krylova, I. V. Lipnevich, V. P. Egorova and A. S. Babenka, *Int. J. Mod. Phys. B* **32** (2018) 1840033.
8. H. V. Grushevskaya, N. G. Krylova, I. V. Lipnevich, T. I. Orekhovskaja, V. P. Egorova and B. G. Shulitski, *Int. J. Mod. Phys. B* **30** (2016) 1642018.
9. H. V. Grushevskaya, N. G. Krylova, I. V. Lipnevich, T. I. Orekhovskaja and B. G. Shulitski, Cell monolayer functioning detection based on quantum polarization effects in Langmuir–Blodgett multi-walled carbon nanotubes films, in *Nanomaterials for Security*, NATO Science for Peace and Security, Series A: Chemistry and Biology, eds. J. Bonca and S. Kruchinin (Springer, Dorchester, 2016), pp. 89–99.
10. H. V. Grushevskaya, N. G. Krylova, I. V. Lipnevich, A. S. Babenka, V. P. Egorova and R. F. Chakukov, *Semiconductors* **52**(14) (2018) 1836.
11. D. J. Griffiths, *Introduction to Electrodynamics*, 4th edn. (Cambridge University Press, Cambridge, 2017).
12. L. P. Kadanoff and G. Baym, *Quantum Statistical Mechanics* (W. A. Benjamin, New York, 1962).
13. H. P. R. Frederikse, Polarizabilities of atoms and ions in solids, in *Handbook of Chemistry and Physics*, 84th edn. (Boca Raton, CRC Press, 2004), pp. 12–17.
14. V. D. Kraeft, D. Kremp, W. Ebeling and G. Röpke, *Quantum Statistics of Charged Particle Systems* (Akademie, Berlin, 1986).
15. B. Prescott, W. Steinmetz and G. J. Thomas Jr., *Biopolymers* **23** (1984) 235.

H. V. Grushevskaya et al.

16. V. S. Gorelik, L. I. Zlobina, A. S. Krylov, V. P. Sverbil and P. P. Sverbi, *Phys. Wave Phenom.* **24**(4) (2016) 272.
17. W. L. Peticolas, Raman spectroscopy of DNA and protein, in *Methods in Enzymology*, Vol. **246** (Academic Press, Cambridge, 1995), pp. 329–416, Chap. 17.
18. C. Otto, T. J. J. van den Tweel, F. F. M. de Mul and J. Greve, *J. Raman Spectrosc.* **17** (1986) 289.
19. M. Kulkarni and A. Mukherjee, *Prog. Biophys. Mol. Biol.* **128** (2017) 63.
20. G. P. Zhizhina and E. F. Oleinik, *Russ. Chem. Rev.* **41** (1972) 258 (in Russian).
21. A. S. Egorov, V. P. Egorova, H. V. Grushevskaya, N. G. Krylova, I. V. Lipnevich, T. I. Orekhovskaya and B. G. Shulitsky, *Lett. Appl. NanoBioScience* **5**(1) (2016) 346.
22. A. S. Babenko, H. V. Grushevskaya, N. G. Krylova, I. V. Lipnevich, V. P. Egorova and R. F. Chakukov, Nanopore-penetration sensing effects for target DNA sequencing via impedance difference between organometallic-complex-decorated carbon nanotubes with twisted single-stranded or double-stranded DNA, in *Advanced Nanomaterials for Detection of CBRN*, NATO Science for Peace and Security, Series A: Chemistry and Biology, eds. J. Bonca and S. Kruchinin (Springer, Dorchester, 2020), pp. 247–258.
23. M. Gąsior-Głogowska, K. Malek, G. Zajaca and M. Baranska, *Analyst* **141** (2016) 291.
24. L. Wang, N. Lu, Sh. Huang, M. Wang, X.-M. Chen and H. Yang, *CCS Chem.* **3** (2021) 1787.
25. V. P. Egorova, H. V. Grushevskaya, N. G. Krylova, E. V. Vaskovtsev, A. C. Babenka, G. G. Krylov, I. V. Anufreyonak and S.Yu. Smirnov, *Int. J. Nonlinear Phenom. Complex Syst.* **26** (2023) 191.
26. H. Grushevskaya and G. Krylov, *Quantum Rep.* **4** (2022) 1.
27. H. Grushevskaya, A. Timoshchenko and I. Lipnevich, *Nanomaterials* **13** (2023) 410.
28. L. Wang, N. An, X. He, X. Zhang, A. Zhu, B. Yao and Ya. Zhang, *Nanomaterials* **12** (2022) 2097.
29. A. N. Tcypkin, E. A. Ponomareva, S. E. Putilin, S. V. Smirnov, S. A. Shtumpf, M. V. Melnik, E. Yiwen, S. A. Kozlov and X.-Ch. Zhang, *Opt. Express* **27** (2019) 15486.
30. P. D. Profio, V. Canale, M. Ciulla, A. Fontana, L. Madia, M. Zampato and S. Carminati, *ACS Sustain. Chem. Eng.* **10** (2022) 4780.
31. V. Balos, N. K. Kaliannan, H. Elgabarty, M. Wolf, T. D. Kühne and M. Sajadi, *Nat. Chem.* **14** (2022) 1031.
32. L. A. Falkovsky and A. A. Varlamov, *Eur. Phys. J.* **56** (2007) 281.
33. R. A. D. de Faria, L. G. D. Heneine, T. Matencio and Y. Messaddeq, *Int. J. Biosen. Bioelectron.* **5** (2019) 29.
34. S. P. Repetsky, I. G. Vyshyvana, S. P. Kruchinin and S. Bellucci, *Sci. Rep.* **8** (2018) 9123.
35. S. P. Repetsky, I. Vyshyvana, Y. Nakazawa, S. Kruchinin and S. Bellucci, *Materials* **12** (2019) 524.
36. C. Gautier, Ch. Esnault, Ch. Cougnon, J.-F. Pilard, N. Casse and B. Chénais, *J. Electroanal. Chem.* **610** (2007) 227.
37. H. V. Grushevskaya, N. G. Krylova, I. V. Lipnevich, T. I. Orekhovskaja and B. G. Shulitski, *Adv. Mater. Lett.* **8** (2017) 531.